Afterslip Enhanced Aftershock Activity During the 2017 Earthquake Sequence Near Sulphur Peak, Idaho

Keith D. Koper[1] iD, Kristine L. Pankow[1] iD, James C. Pechmann[1] iD, J. Mark Hale[1] iD, Relu Burlacu[1], William L. Yeck[2] iD, Harley M. Benz[2] iD, Robert B. Herrmann[3], Daniel T. Trugman[4] iD, and Peter M. Shearer[5] iD

[1]Department of Geology and Geophysics, University of Utah, Salt Lake City, UT, USA, [2]U.S. Geological Survey, National Earthquake Information Center, Denver, CO, USA, [3]Department of Earth and Atmospheric Sciences, Saint Louis University, St. Louis, MO, USA, [4]Earth and Environmental Sciences Division, Los Alamos National Laboratory, Los Alamos, NM, USA, [5]Scripps Institution of Oceanography, University of California San Diego, La Jolla, CA, USA

Abstract An energetic earthquake sequence occurred during September to October 2017 near Sulphur Peak, Idaho. The normal-faulting M_w 5.3 mainshock of 2 September 2017 was widely felt in Idaho, Utah, and Wyoming. Over 1,000 aftershocks were located within the first 2 months, 29 of which had magnitudes ≥ 4.0 M_L. High-accuracy locations derived with data from a temporary seismic array show that the sequence occurred in the upper (<10 km) crust of the Aspen Range, east of the northern section of the range-bounding, west-dipping East Bear Lake Fault. Moment tensors for 77 of the largest events show normal and strike-slip faulting with a summed aftershock moment that is 1.8–2.4 times larger than the mainshock moment. We propose that the unusually high productivity of the 2017 Sulphur Peak sequence can be explained by aseismic afterslip, which triggered a secondary swarm south of the coseismic rupture zone beginning ~1 day after the mainshock.

Plain Language Summary During the fall of 2017, an energetic sequence of earthquakes was recorded in southeastern Idaho. The mainshock had a moment magnitude of M_w 5.3, yet thousands of aftershocks were detected. We found that the unusually high productivity of this earthquake sequence can be explained by extra sliding that occurred just after the mainshock. This extra sliding happened too slowly to generate seismic waves, but it was large enough to alter the stress in the crust such that the extra aftershocks were created. Our finding suggests that in this region of Idaho, some of the strain that is built up by tectonic forces is released in slow-slip or creep events. This discovery will ultimately lead to more accurate forecasts of seismic hazard in the region.

1. Introduction

On 2 September 2017, an M_w 5.3 normal-faulting earthquake occurred about 12 km east of Soda Springs, Idaho, near Sulphur Peak (origin time of 23:56:52 UTC, epicenter of 42.647°N, 111.449°W, depth of 9.5 km; U.S. Geological Survey, 2017). It was widely felt throughout southeastern Idaho, northern Utah, and western Wyoming, though it caused little damage. The earthquake was located in the Intermountain Seismic Belt (ISB), a diffuse band of seismicity in the western United States that stretches from northwestern Arizona to northwestern Montana (Figure 1; Smith & Arabasz, 1991). The ISB is dominated by extensional tectonics with the minimum horizontal stress oriented roughly east-west. Like previous earthquake sequences in the southeastern Idaho portion of the ISB—such as the M_w 5.7 Draney Peak sequence of 1994 (Brumbaugh, 2001)—the 2017 Sulphur Peak sequence was very energetic. Nine foreshocks with coda duration magnitudes (M_C) of 1.3–4.1 were recorded in the 34 min prior to the mainshock, and over 1,000 aftershocks were located within the first 2 months.

The 2017 Sulphur Peak sequence is notable in at least two respects. First, it appears to be a repeat of two earlier seismic sequences, one in the summer of 1960 and the other in the fall of 1982. Between 23 July and 26 August 1960, the U.S. Coast and Geodetic Survey reported instrumental locations for 17 earthquakes (maximum intensity of MMI VI) in southeast Idaho (longitudes of 111.2–111.7°W, latitudes of 42.3–42.6°N; Talley & Cloud, 1962). The locations are precise to only 0.1° or 0.5° but felt reports confirm that the sequence happened near Soda Springs and had many more events. During the fall 1982 sequence, following the largest earthquake of M_L 4.7, a temporary network of 19 stations was deployed in the epicentral region and
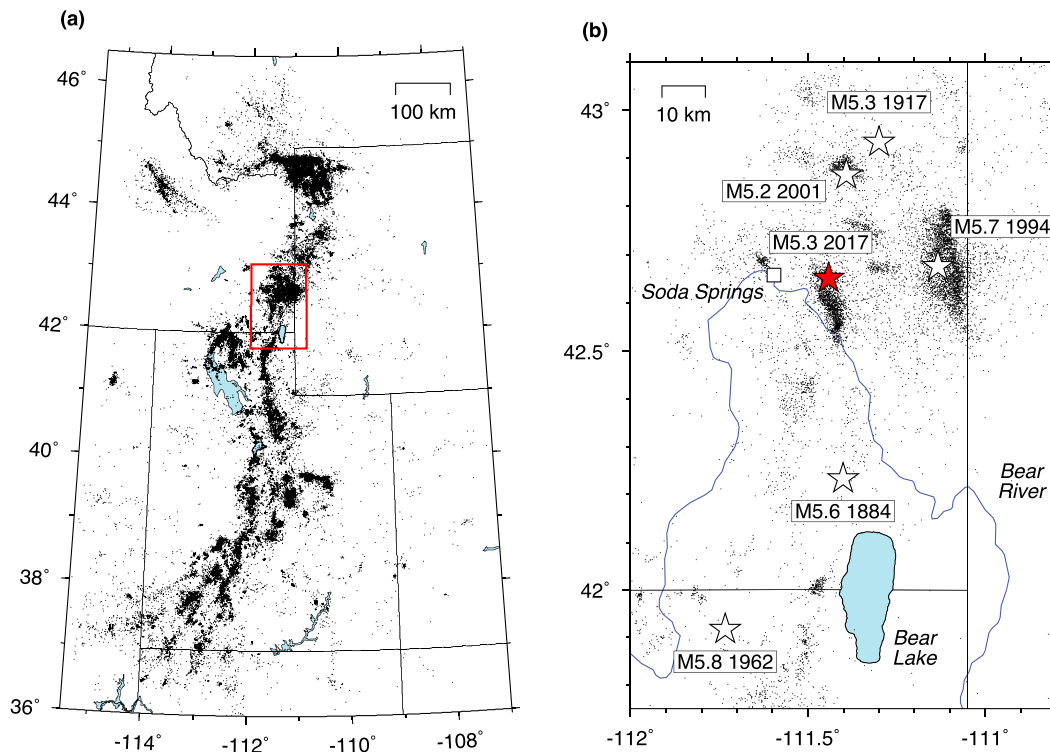
Figure 1. (a) Seismicity in the University of Utah Seismograph Stations event catalog from 1 January 1981 through 31 December 2017. Most of the earthquakes are concentrated within the Intermountain Seismic Belt, which is the 100 to 200-km-wide zone of seismicity trending south-southwest to north-northeast near the center of the map area (Smith & Arabasz, 1991). The red box outlines the region shown to the right. (b) Seismicity in the region surrounding the 2017 Sulphur Peak sequence. Earthquakes with magnitude larger than $M5$ are shown with white stars, and the 2017 Sulphur Peak mainshock is shown with a red star. Locations and magnitudes of pre-1981 earthquakes are from Arabasz et al. (2016).

recorded approximately 2,000 earthquakes in 11 days (Smith et al., 1983). A joint hypocentral relocation technique was applied to 219 of the best-recorded earthquakes (Arabasz & Julander, 1986), and the resulting epicentral zone overlaps the 2017 sequence (Figure 2).

A second notable feature of the 2017 Sulphur Peak sequence is that it occurred beneath the Aspen Range to the east of the west-dipping northern section of the East Bear Lake Fault (EBLF), which bounds the range (Figure 2). The EBLF is the master normal fault in the region. A geological cross section by Evans et al. (2003) near the 1884 epicenter (Figure 1b) shows the EBLF dipping steeply to the west near the surface but becoming listric at depth and merging into the low-angle Home Canyon thrust; however, for seismic hazard analyses, the EBLF and other ISB normal faults are typically assumed to be planar with dips of 50°±15° (Petersen et al., 2014; Wong et al., 2016). Quaternary-age fault scarps are observed along the three sections of the EBLF, and on the southern section, there is paleoseismic evidence for 5–7 surface-rupturing ($M6.8$–7.2) earthquakes in the last 40,000 years, including two in the Holocene (McCalpin, 2003). Recent geodetic observations confirm significant present-day deformation near the EBLF with an extensional strain rate of $6.4 \pm 0.5 \times 10^{-9}$ yr^{-1} (Payne et al., 2012).

Here we document detailed properties of the 2017 Sulphur Peak sequence using data recorded from a network of eight seismographs that was temporarily deployed in the source region from 6 September through 26 October 2017. We combine the local seismic data with data from several permanent regional seismic networks to generate high-accuracy locations and magnitudes for 1,048 earthquakes. We explore differences in locations among multiple algorithms to evaluate the final locations. We also invert regional distance waveforms for moment tensors of 77 of the largest events. Both frequency-magnitude statistics and cumulative moment calculations indicate that the 2017 Sulphur Peak sequence was substantially more energetic than a typical mainshock-aftershock sequence. Motivated by these observations, we explore mechanisms of aftershock triggering that can explain the anomalously high productivity of the 2017 Sulphur Peak sequence.
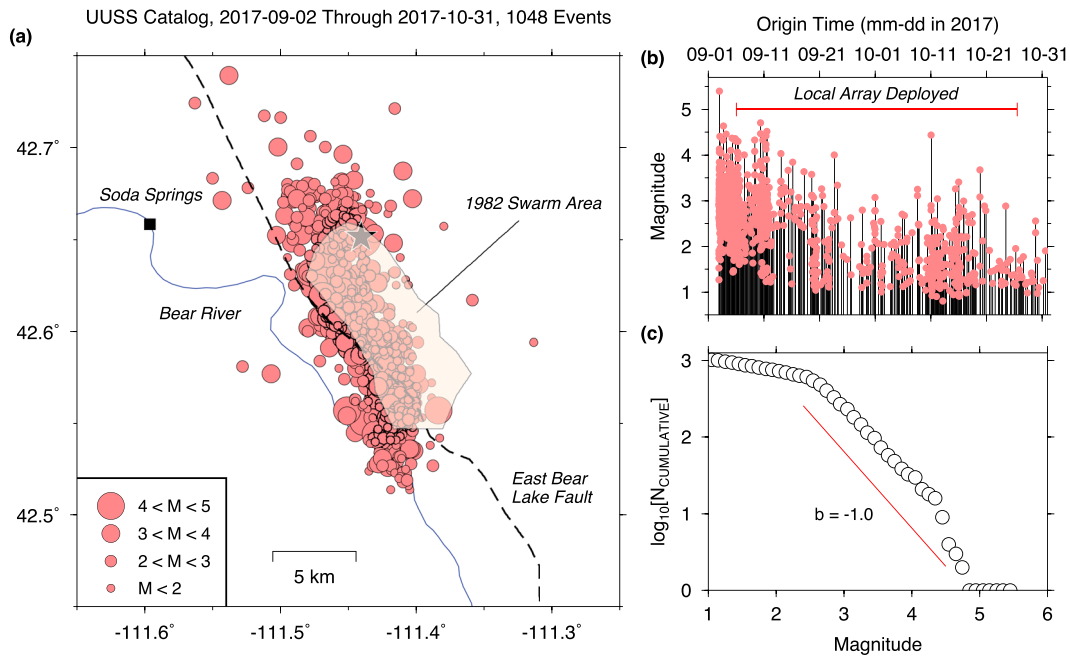
Figure 2. (a) University of Utah Seismograph Stations (UUSS) locations of 1,048 earthquakes that occurred between 2 September 2017 and 31 October 2017. The M_L 5.4 mainshock is shown with a black star. The surface trace of the East Bear Lake Fault (black dashed line) is from Breckenridge et al. (2003). The light orange polygon shows the area covered by the 1982 sequence from 15–26 October (Arabasz & Julander, 1986). (b) Magnitude-time evolution of the seismicity. (c) Cumulative frequency-magnitude curve. A red line with a slope of −1 is shown for reference. Note the anomalously large number of $M4+$ events. Magnitudes in all three panels are the UUSS preferred magnitude, which is local magnitude (M_L) for nearly all of the events larger than ~$M2.5$ and either M_L or coda duration magnitude (M_C) for smaller events.

2. Seismic Data for the 2017 Sulphur Peak, Idaho, Sequence

Nine permanent seismic networks (Table S1) operate 65 high-gain seismometers within 220 km of the 2017 Sulphur Peak mainshock, for which data are openly available in near real time (www.iris.edu/dmc); however, only three permanent stations are within 50 km of the epicentral area and there are significant azimuthal gaps to the west and east-southeast (Figure S1a). To achieve high-accuracy hypocentral locations, the University of Utah Seismograph Stations (UUSS) and the U.S. Geological Survey (USGS) partnered with the Idaho Geological Survey to deploy eight temporary seismographs in the epicentral region within 4–10 days of the mainshock (Figure S1b and Table S2) including two strong-motion stations (Network UU; stations: ASI4 and ASI5) and six broadband plus strong-motion stations (Network GS; stations: ID05, ID06, ID07, ID08, ID09, and ID10). All eight stations transmitted data in near real time that were incorporated into UUSS and USGS monitoring operations. The six GS stations were demobilized 24–26 October 2017, while the two UU stations remain active, although ASI5 was moved 90 m and renamed ASI6. Data quality from the temporary stations is high, and we show waveforms from a typical local event in the supplement (Figure S2).

3. Earthquake Locations and Magnitudes

We present the UUSS locations and magnitudes of 1,048 earthquakes in the 2017 Sulphur Peak sequence in Figure 2. UUSS analysts manually picked P and S wave arrival times which we used to determine hypocenters with HYPOINVERSE (Klein, 2002) and a 1-D velocity model (Table S3) created during a study of the nearby 1994 Draney Peak earthquake sequence (Brumbaugh, 2001). We calculated coda duration magnitudes (M_C) for >98% of the earthquakes and local magnitudes (M_L) for 84%, including all but four of the 548 events larger than ~2.5 M_L, which we estimate to be the magnitude of completeness. Details of the procedures used by UUSS to calculate magnitudes are available in Pechmann et al. (2006) for M_C and in Pechmann et al. (2007) for M_L. The two magnitude scales are designed to be seamless, and for earthquakes in the Utah region that occur deeper than 3–4 km, the average M_L-M_C is near zero (Koper et al., 2016).

The deployment of local seismometers greatly reduced location uncertainties. Beginning on 9 September 2017, when local data started to be routinely incorporated into the processing pipeline, the median of the standard errors in horizontal distance (ehr) dropped from 0.7 to 0.4 km, and the median of the standard errors in depth (ehz) dropped from 4.4 to 0.6 km. Because the Sulphur Peak sequence was independently processed by the USGS (Figure S3) with a different velocity model, a different location algorithm, and different sets of arrival time picks, we can use the differences between the two catalogs to estimate the systematic, model-based uncertainties in the hypocenters. As shown in Figure S4, the differences in epicenter and depth for the 436 events common to both catalogs have median values of 1.60 and 2.02 km, respectively. If we limit the comparison to the 183 common events located with temporary station data after 8 September (Figure S5), the median values drop to 1.07 km (epicenter) and 1.67 km (depth).

The small uncertainties in absolute hypocenters imply that two first-order observations about the 2017 Sulphur Peak sequence are robust. First, most and perhaps all of the events are to the east of the west-dipping EBLF, in its footwall block. The surface expression of this fault strikes NW-SE, following the trend of the Bear River. The northern events are clearly east of this feature, while the southern events are also likely in the footwall because of the westward dip of the fault zone. Second, the events are confined to the upper crust, with a median depth of 6.0–7.3 km and a maximum depth of ~10–12 km below sea level (Figure S6). These observations are similar to those made for the 1982 sequence (Arabasz & Julander, 1986; Smith et al., 1983). The space-time pattern of seismicity in the 2017 sequence is also similar to the 1982 sequence in that it migrates from north to south (Figure S7).

The pattern of southward migration, and other fine details of the space-time distribution of the 2017 seismicity, can be better imaged with techniques that use differential arrival times to jointly locate hypocenters in a relative sense. Here we use two approaches to generate high-accuracy relative relocations for the 2017 Sulphur Peak sequence. The first approach is a multiple-event, hypocentroidal decomposition method known as MLOC (Bergman & Solomon, 1990; Karasözen et al., 2016), which splits the location problem into that for a cluster hypocentroid and separate earthquake cluster-vectors relative to that hypocentroid. Only near-source observations are used when locating the hypocentroid, which reduces absolute location bias introduced by unmodeled velocity structures. The second approach, known as GrowClust (Trugman & Shearer, 2017), is likewise a cluster-based relative relocation algorithm, but one that incorporates differential arrival times measured via waveform cross correlation. The differential arrival times are powerful constraints and, similar to HypoDD (Waldhauser, 2000), GrowClust can help resolve linear and planar structures from within diffuse clouds of seismicity.

In Figure S8, we compare the epicenters from our four earthquake catalogs: the USGS absolute locations, the UUSS absolute locations, the MLOC relative relocations, and the GrowClust relative relocations. We used the UUSS absolute locations as starting points for both relative relocation approaches. The general pattern of seismicity is similar in each case; however, the finest details appear in the GrowClust relocations, which we present in Figure 3. As expected, the locations remain mostly to the east of the EBLF, in the upper crust of the Aspen Range, and overlapping the western portion of the source area of the 1982 sequence. The detailed pattern of the 2017 seismicity remains the same even if we consider only those events that occurred after 8 September, when local arrival times were routinely included in the locations (Figure S9).

As shown in Figure 3, the seismicity decreases abruptly for depths greater than 7–8 km, which puts them in the uppermost 10 km of the crust after accounting for the average surface elevation of ~2 km. This feature was inherited from the original UUSS locations. We confirmed that it is not an artifact by recomputing the UUSS locations in HYPOINVERSE with different starting depths, a slightly different velocity model, and changes to the distance weighting of *P* and *S* arrival times. In all cases, there remained a sharp drop-off in seismicity below a depth of 8–10 km. A similar pattern was observed during the 1982 sequence, which further suggests that the drop-off in the 2017 sequence is not a processing artifact. Arabasz and Julander (1986) reported that 84% of the earthquakes with good locations in 1982 occurred shallower than 7 km and only 15% occurred at depths of 7–10 km. They interpret the seismicity drop-off at 7–8 km with the Meade Thrust and the near cessation in seismicity at 10–11 km with the Absaroka Thrust. The Meade Thrust and Absaroka Thrust are low-angle detachments that formed under compressive stress conditions during the Mesozoic-Paleogene, and Arabasz and Julander (1986) hypothesized that these structural discontinuities,
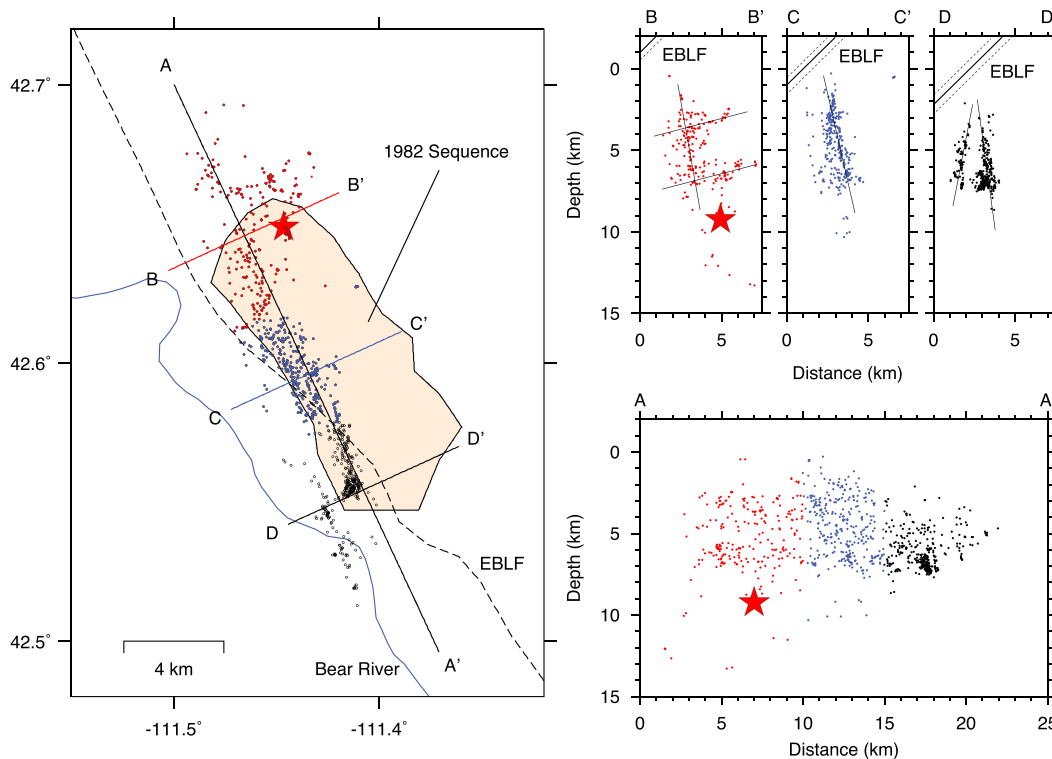
Figure 3. High-resolution hypocentral locations computed with the relative relocation technique GrowClust (Trugman & Shearer, 2017). The dots are colored as a function of distance along A-A' to better highlight how fault morphology changes along strike. The location of the mainshock is shown with a red star, and depth is plotted relative to sea level. Elevation in the region is approximately 2 km. The light orange polygon shows the location of the 1982 earthquake sequence. The straight, light black lines in the upper right cross sections indicate planar structures that were illuminated by the aftershocks. The low-angle, westward dipping faults may be reactivated thrust sheets, as shown in Evans et al. (2003). The dark black lines (bracketed by thin dashed lines) show the location of the East Bear Lake Fault (EBLF) at depth assuming a dip of 45° (Collettini & Sibson, 2001).

as opposed to rheological changes, exerted local control on the depth distribution of upper-crustal seismicity in the region.

North of about 42.61°N, near the mainshock, the seismicity extends more broadly in the east-west direction and forms two moderately SW-dipping planes that merge into a steep, NE-dipping plane (Figure 3, red dots). Moving to the southeast, the moderate-dipping planes disappear and only a near-vertical, NE-dipping plane remains (Figure 3, blue dots). Continuing to the southeast, the seismicity forms a steep, NE-dipping plane and then jogs to the southwest and forms a steep, SW-dipping plane that crosses the Bear River in map view (Figure 3, black dots). All of the steeply dipping planar structures have NNW-SSE strikes that are rotated slightly clockwise from the trend of the Bear River Valley and the EBLF.

4. Moment Tensor Inversion of Seismic Waveforms

Three independent research groups reported a total of four moment tensor solutions for the Sulphur Peak mainshock (Table S4). The solutions are similar, with normal or oblique-normal faulting that strikes N-S, centroid depths of 9–15 km, and moment magnitudes of 5.1–5.3 M_w. The scalar moments derived from shorter-period regional waveforms (USGS Regional and SLU) are roughly a factor of 2 smaller than those derived from longer-period teleseismic waveforms (USGS W-phase and gCMT). The three approaches that permit fully deviatoric moment tensors (USGS Regional, USGS W-phase, and gCMT) show negligible nondouble-couple components.

We used the SLU approach described in Herrmann et al. (2011) to invert regional-distance waveforms for moment tensors of the largest foreshock and 74 aftershocks in the 2017 Sulphur Peak sequence. Including the mainshock, this results in a total of 76 moment tensors. The faulting is a mixture of normal and strike-slip; however, the T axis orientations are quite consistent, varying from E-W at the northern edge of the sequence
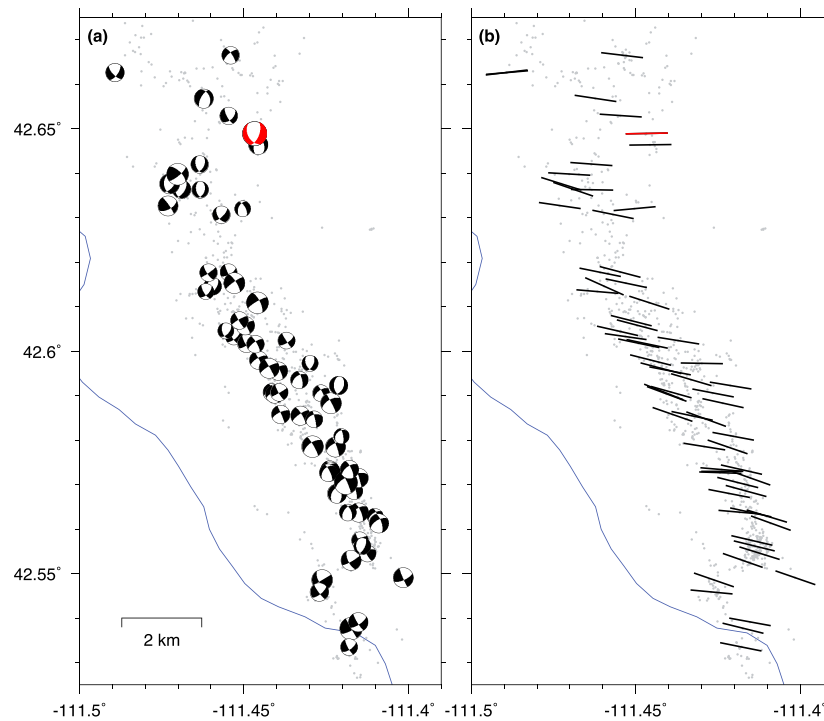
Figure 4. (a) SLU focal mechanisms for 76 of the largest events overlaid on all the GrowClust locations (gray dots). Focal mechanism size is proportional to moment, and the mainshock is shown in red. (b) T axis orientations from SLU focal mechanisms. Length is constant, and the mainshock is shown with red. Note the slight clockwise rotation of the stress axes south of ~42.62°N. The blue line indicates the course of the Bear River.

to ESE-WNW for the central and southern portions of the sequence (Figure 4). Hence, the dominant property of the stress field is an E-W oriented horizontal minimum stress ($\sigma_{H,E-W}$) that is significantly smaller than both the vertical stress, σ_V, and a comparably sized N-S oriented horizontal stress, $\sigma_{H,N-S}$. When $\sigma_V > \sigma_{H,N-S}$, such as in the area around the mainshock, normal faulting results, and when $\sigma_V < \sigma_{H,N-S}$, strike-slip faulting results. The SLU centroid depths vary from 5 to 12 km and track the UUSS focal depths with negligible bias (mean difference of 0.05 km). The moment magnitudes vary from 3.23 to 4.82 M_w and track the UUSS local magnitudes with negligible bias (mean difference of 0.03 units). The unusual strength of the aftershock sequence noted in the introduction is evident in the moment tensor results—the sum of the scalar moments of the 74 aftershocks is 2.4 times that of the (SLU) M_w 5.06 mainshock.

We also estimated moment tensors for the largest foreshock and 75 aftershocks using the USGS procedure for inverting regional waveforms. Including the mainshock, this results in a total of 77 moment tensors. This approach is similar to that of Herrmann et al. (2011); however, it allows for nondouble-couple solutions. There were also minor differences in passbands and trace selection between the SLU and USGS analyses. The USGS moment tensor results are presented in Figure S10. The faulting pattern agrees very well with that from the SLU catalog (Figure 4) with a mix of strike-slip and normal faulting and a similar rotation in T axes from E-W to ESE-WNW from north to south. The USGS centroids are on average 1.45 km shallower than the UUSS focal depths; however, because the SLU centroids did not show a similar bias, we think that is more likely due to the use of different Earth models as opposed to vertical rupture directivity. The USGS moment magnitudes are larger than those from SLU by an average of ~0.03 magnitude units, and the total scalar moment of the aftershocks is 1.8 times that of the (USGS regional) M_w 5.2 mainshock.

5. Discussion

Key observations from the 2017 Sulphur Peak sequence include not only the unusual location within the foot-wall of an active normal fault but also the unusually high aftershock productivity. Within 40 days of the mainshock there were 17 aftershocks with magnitudes larger than the upper bound of 4.2 M_L (mainshock UUSS M_L of 5.4 minus 1.2) expected from Båth's law (Båth, 1965), and 16 of the 17 occurred within 10 days
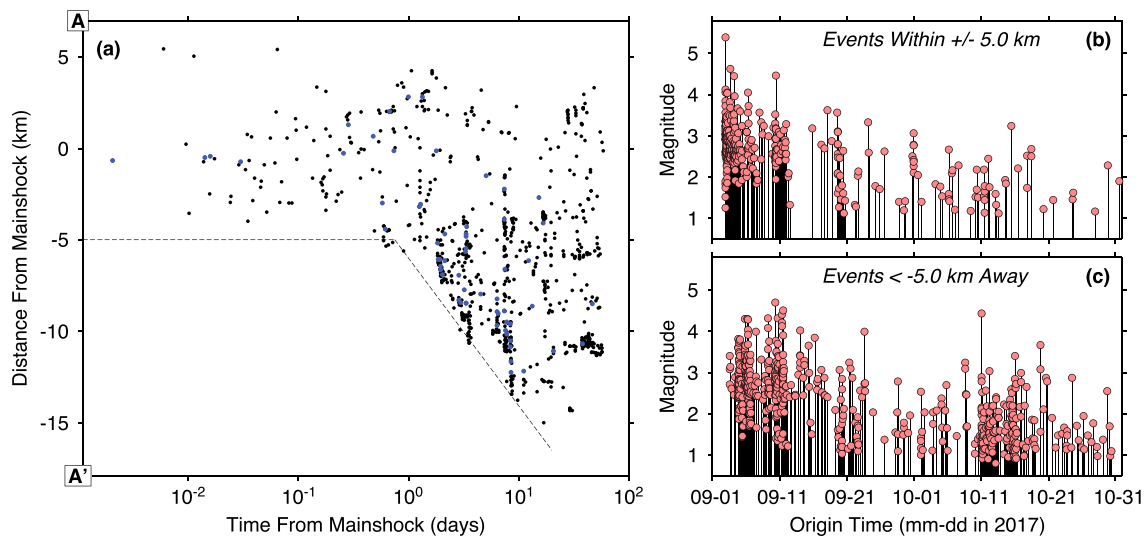
Figure 5. (a) Space-time history of the GrowClust relocated events. Distance on the y axis is calculated along the NNW-SSE oriented A-A' line in Figure 3, with the mainshock epicenter set to 0. The blue circles indicate events with $M_L > 3.5$. Migration to the south begins ~1 day after the mainshock. Separate magnitude-time curves for events (b) north and (c) south of ~42.6°N. This division is slightly south of the red-blue division shown in Figure 3.

of the mainshock. Following Reasenberg and Jones (1994), which assumes that only the stress change from the mainshock drives aftershocks, the expected number of such aftershocks is 0–4 and the probability of observing 16 is just 2.3×10^{-12}. In addition, the cumulative aftershock moment in the 2017 Sulphur Peak sequence is 1.8–2.4 times as large as the mainshock moment, whereas the cumulative aftershock moment of typical crustal earthquake sequences has been estimated as 0.033–0.21 (Kagan & Houston, 2005) and 0.0014–0.20 (Wiens & McGuire, 2000) times as large as the mainshock moment.

At the same time, the 2017 Sulphur Peak sequence had a clear mainshock that was separated by 0.7 magnitude units and ~8 days from the largest aftershock—an M_L 4.7 event on 10 September 2017. This observation is in contrast to truly swarm-like sequences such as the 2012 Brawley, California, sequence in which the three largest earthquakes had magnitudes of 5.3 M_w, 4.9 M_w, and 5.4 M_w and occurred within a time span of 90 min (Hauksson et al., 2013) or the 2010 Yellowstone swarm, which had several days of increasing magnitude earthquakes and a "mainshock" that was only ~0.1–0.2 magnitude units larger than the next largest aftershock (Shelly et al., 2013). Therefore, we prefer to describe the 2017 Sulphur Peak sequence as a hybrid or Type II (Mogi, 1963) sequence that has properties of both mainshock-aftershock sequences and swarms.

Using the final locations obtained from GrowClust (Figure 3), we illustrate the space-time migration of aftershocks in Figure 5. During the first ~1 day the aftershocks are confined to within ~5 km NNW and SSE of the mainshock, in the area north of ~42.6°N that we interpret as the coseismic rupture zone (Pegler & Das, 1996; Tajima & Kanamori, 1985). The time-magnitude plot for earthquakes north of ~42.6°N is similar to that of a typical mainshock-aftershock sequence (Figure 5b). Beginning ~1 day after the mainshock, the aftershock migration rate increases and the sequence migrates about 10 km SSE over the following 10 days. The time-magnitude plot for these more distant aftershocks, south of ~42.6°N, is similar to that of a swarm as it has no outstanding principal event (Figure 5c). The relatively rapid migration rate of 1 km/d is consistent with aftershocks triggered by afterslip (e.g., Hauksson et al., 2017; Perfettini et al., 2018; Ross et al., 2017).

A close-up of aftershock migration in the first 10 days reveals that several streaks of extremely rapidly migrating events are embedded within the overall trend of ~1 km/d (Figure S11). We overlay the trajectories expected for a fluid-driven process using the relationship $r = (4\pi Dt)^{1/2}$, where r is distance, D is hydraulic diffusivity, and t is time (Shapiro et al., 1997). Diffusivity values of 20–30 m²/s are required to match our observations if the fluid source is assumed to start at the time and location of the mainshock, and values of 6–10 m²/s are required if the fluid source is shifted in time and space to match the beginning of the southern migration. These diffusivities are lower bounds because we use horizontal along-strike distance for r; using true three-dimensional distance would lead to larger diffusivities. Commonly observed diffusivity values

for fluid-induced sequences are in the range of 0.2–2.0 m^2/s (Shelly et al., 2013); hence, we prefer afterslip as the driving mechanism for the southern migration of aftershocks in the 2017 Sulphur Peak sequence.

Dividing the 2017 Sulphur Peak sequence into a conventional aftershock sequence and a swarm-like sequence helps to explain its anomalously high productivity. In the aftershock-type sequence, north of ~42.6°N, there are only three events with magnitudes larger than Båth's law bound in the first 10 days (Figure 5b), which is consistent with the expectations of Reasenberg and Jones (1994). Analysis of the SLU cumulative moment indicates that the northern aftershocks account for 0.6 times the mainshock moment, while the cumulative moment for the southern swarm events is 1.8 times the mainshock moment. The division of the Sulphur Peak sequence into distinct subsequences is also consistent with the change in fault morphology—with narrower, steeply dipping planar structures south of ~42.6°N (Figures 3 and S9)—and the slight (~10°) clockwise rotation of the horizontal stress axes for earthquakes south of ~42.6°N (Figures 4 and S10).

6. Conclusions

High-resolution locations of the 2017 Sulphur Peak, Idaho, earthquake sequence show activation of at least two low-angle (~25°–30°) westward dipping planes and high-angle (~80°) eastward and westward dipping planes, all of which are located in the footwall block of the EBLF. The orientations of these planes are roughly consistent with the nodal planes of the mainshock and many of the large aftershocks. We interpret the low-angle planar structures as reactivated thrust sheets that were originally created during compressional orogenic episodes in the Mesozoic-Paleogene. Several such thrust sheets (e.g., Meade, Absaroka, and Home Canyon) have been imaged in the region with reflection seismology (Evans, 1991; Evans et al., 2003).

Magnitude-time and cumulative moment calculations indicate that the 2017 Sulphur Peak sequence was too energetic to be explained as a standard mainshock-aftershock sequence. The localized distribution of aftershocks within ~5 km of the mainshock is consistent with response to coseismic slip on the rupture plane of a M_w 5.3 earthquake (e.g., Ben-Zion & Lyakhovsky, 2006; Dietrich, 1994); however, the rapid spatial expansion of aftershocks over 10 km to the SE requires an additional driving force. The two most commonly invoked explanations for excessive, swarm-like aftershocks are fluid diffusion (e.g., Nur & Booker, 1972; Parotidis et al., 2003; Shelly et al., 2013) and aseismic afterslip (Perfettini et al., 2018; Perfettini & Avouac, 2004). The 2017 Sulphur Peak sequence appears to have migrated to the SE too quickly to be explained solely by fluid diffusion, and we prefer aseismic afterslip as the primary driving force.

Although no GPS or strain meter data are available to test this idea directly, the 2017 Sulphur Peak aftershock migration rates are similar to those of other seismic sequences with confirmed afterslip (e.g., Canitano et al., 2018), as well as creep events in California (e.g., Linde et al., 1996; Lohman & McGuire, 2007). The combination of afterslip in the 2017 Sulphur Peak sequence and the cyclic/repeating nature of seismicity in this area—as indicated by the previous energetic, co-located sequences in 1960 and 1982—suggests that southeastern Idaho might be a region with slow-slip or creep (Peng & Gomberg, 2010), a style of deformation that is consistent with the relatively high strain rates (Payne et al., 2012; Schmeelk et al., 2017) and high heat flow (Blackwell et al., 2011) in the region.

References

Arabasz, W. J., & Julander, D. R. (1986). Geometry of seismically active faults and crustal deformation within the Basin and Range-Colorado Plateau transition in Utah. *Geological Society of America Special Papers*, *208*, 43–75. https://doi.org/10.1130/SPE208-p43

Arabasz, W. J., Pechmann, J. C., & Burlacu, R. (2016). A uniform moment magnitude earthquake catalog and background seismicity rates for the Wasatch Front and surrounding Utah region, appendix E of Working Group on Earthquake Probabilities, Earthquake probabilities for the Wasatch Front region in Utah, Idaho, and Wyoming, Utah Geological Survey Miscellaneous Publication 16–3, p. E-1 to E-26 plus 10 electronic supplements.

Båth, M. (1965). Lateral inhomogeneities of the upper mantle. *Tectonophysics*, *2*(6), 483–514. https://doi.org/10.1016/0040-1951(65)90003-X

Ben-Zion, Y., & Lyakhovsky, V. (2006). Analysis of aftershocks in a lithospheric model with seismogenic zone governed by damage rheology. *Geophysical Journal International*, *165*(1), 197–210. https://doi.org/10.1111/j.1365-246X.2006.02878.x

Bergman, E. A., & Solomon, S. C. (1990). Earthquake swarms on the Mid-Atlantic Ridge: Products of magmatism or extensional tectonics? *Journal of Geophysical Research*, *95*(B4), 4943–4965. https://doi.org/10.1029/JB095iB04p04943

Blackwell, D., Richards, M., Frone, Z., Batir, J., Ruzo, A., Dingwall, R., & Williams, M. (2011). Temperature-at-depth maps for the conterminous U. S. and geothermal resource estimates. *GRC Transactions*, *35*, 1545–1550.

Breckenridge, R. M., Lewis, R. S., Adema, G. W., & Weisz, D. W. (2003). Miocene and younger faults in Idaho, Idaho Geological Survey Map 8, scale 1:1,000,000.

Brumbaugh, D. A. (2001). The 1994 Draney Peak, Idaho, Earthquake Sequence: Focal Mechanisms and Stress Field Inversion, M.S. thesis, University of Utah, 157 p.

Canitano, A., Godano, M., Hsu, Y.-J., Lee, H.-M., Linde, A. T., & Sacks, S. (2018). Seismicity controlled by a frictional afterslip during a small-magnitude seismic sequence ($M_L<5$) on the Chihshang Fault, Taiwan. *Journal of Geophysical Research: Solid Earth*, *123*, 2003–2018. https://doi.org/10.1002/2017JB015128

Collettini, C., & Sibson, R. H. (2001). Normal faults, normal friction? *Geology*, *29*(10), 927–930. https://doi.org/10.1130/0091-7613(2001)029<0927:NFNF>2.0.CO;2

Dietrich, J. (1994). A constitutive law for rate of earthquake production and its application to earthquake clustering. *Journal of Geophysical Research*, *99*, 2156–2202.

Evans, J. P. (1991). Structural setting of seismicity in Northern Utah, contract report 91–15, Utah Geological Survey, 37 p.

Evans, J. P., Martindale, D. C., & Kendrick, R. D. Jr. (2003). Geologic setting of the 1884 Bear Lake, Idaho, earthquake: Rupture in the hanging wall of a basin and range normal fault revealed by historical and geological analyses. *Bulletin of the Seismological Society of America*, *93*(4), 1621–1632. https://doi.org/10.1785/0120020159

Hauksson, E., Meier, M.-A., Ross, Z. E., & Jones, L. M. (2017). Evolution of seismicity near the southernmost terminus of the San Andreas Fault: Implications of recent earthquake clusters for earthquake risk in southern California. *Geophysical Research Letters*, *44*, 1293–1301. https://doi.org/10.1002/2016GL072026

Hauksson, E., Stock, J., Bilham, R., Boese, M., Chen, X., Fielding, E. J., et al. (2013). Report on the August 2012 Brawley earthquake swarm in Imperial Valley, Southern California. *Seismological Research Letters*, *84*(2), 177–189. https://doi.org/10.1785/0220120169

Herrmann, R. B., Benz, H., & Ammon, C. J. (2011). Monitoring the earthquake source process in North America. *Bulletin of the Seismological Society of America*, *101*(6), 2609–2625. https://doi.org/10.1785/0120110095

Kagan, Y. Y., & Houston, H. (2005). Relation between mainshock rupture process and Omori's law for aftershock moment release rate. *Geophysical Journal International*, *163*(3), 1039–1048. https://doi.org/10.1111/j.1365-246X.2005.02772.x

Karasözen, E., Nissen, E., Bergman, E. A., Johnson, K. L., & Walters, R. J. (2016). Normal faulting in the Simav graben of western Turkey reassessed with calibrated earthquake relocations. *Journal of Geophysical Research: Solid Earth*, *121*, 4553–4574. https://doi.org/10.1002/2016JB012828

Klein, F. W. (2002). User's guide to HYPOINVERSE-2000, a Fortran program to solve for earthquake locations and magnitudes, open file report 2002–171, U.S. Geological Survey, 123 p.

Koper, K. D., Pechmann, J. C., Burlacu, R., Pankow, K. L., Stein, J., Hale, J. M., et al. (2016). Magnitude-based discrimination of man-made seismic events from naturally occurring earthquakes in Utah, USA. *Geophysical Research Letters*, *43*, 10,638–10,645. https://doi.org/10.1002/2016GL070742

Linde, A. T., Gladwin, M. T., Johnston, M. J. S., Gwyther, R. L., & Bilham, R. G. (1996). A slow earthquake sequence on the San Andreas Fault. *Nature*, *383*(6595), 65–68. https://doi.org/10.1038/383065a0

Lohman, R. B., & McGuire, J. J. (2007). Earthquake swarms driven by aseismic creep in the Salton Trough, California. *Journal of Geophysical Research*, *112*, B04405. https://doi.org/10.1029/2006JB004596

McCalpin, J. P. (2003). Neotectonics of Bear Lake Valley, Utah and Idaho; a preliminary assessment. In *Paleoseismology of Utah* (Vol. 12, p. 43). miscellaneous publication 03–4. Salt Lake City, UT: Utah Geological Survey.

Mogi, K. (1963). 38. Some discussions on aftershocks, foreshocks and earthquake swarms—The fracture of a semi-infinite body caused by an inner stress origin and its relation to the earthquake phenomena (third paper). *Bulletin of the Earthquake Research Institute*, *41*, 615–658.

Nur, A., & Booker, J. R. (1972). Aftershocks caused by pore fluid flow? *Science*, *25*, 885–887.

Parotidis, M., Rothert, E., & Shapiro, S. A. (2003). Pore-pressure diffusion: A possible triggering mechanism for the earthquake swarms 2000 in Vogtland/NW-Bohemia, Central Europe. *Geophysical Research Letters*, *30*(20), 2075. https://doi.org/10.1029/2003GL018110

Payne, S. J., McCaffrey, R., King, R. W., & Katterhorn, S. A. (2012). A new interpretation of deformation rates in the Snake River Plain and adjacent basin and range regions based on GPS measurements. *Geophysical Journal International*, *189*(1), 101–122. https://doi.org/10.1111/j.1365-246X.2012.05370.x

Pechmann, J. C., Bernier, J. C., Nava, S. J., & Terra, F. M. (2006). Correction of systematic time-dependent coda magnitude errors in the Utah and Yellowstone National Park region earthquake catalogs, 1981–2001, Appendix C in Arabasz, W. J., R. B. Smith, J. C. Pechmann, K. L. Pankow, and R. Burlacu, Integrated Regional and Urban Seismic Monitoring – Wasatch Front Area, Utah and Adjacent Intermountain Seismic Belt, Final Tech. Rept., U.S. Geological Survey Cooperative Agreement 04HQAG0014, 137 pp. Retrieved from http://earthquake.usgs.gov/research/external/reports/04HQAG0014.pdf

Pechmann, J. C., Nava, S. J., Terra, F. M., & Bernier, J. C. (2007). Local magnitude determinations for Intermountain Seismic Belt earthquakes from broadband digital data. *Bulletin of the Seismological Society of America*, *97*(2), 557–574. https://doi.org/10.1785/0120060114

Pegler, G., & Das, S. (1996). Analysis of the relationship between seismic moment and fault length for large crustal strike-slip earthquakes between 1977–92. *Geophysical Research Letters*, *23*(9), 905–908. https://doi.org/10.1029/96GL00963

Peng, Z., & Gomberg, J. (2010). An integrated perspective of the continuum between earthquakes and slow-slip phenomena. *Nature Geoscience*, *3*(9), 599–607. https://doi.org/10.1038/ngeo940

Perfettini, H., & Avouac, J.-P. (2004). Postseismic relaxation driven by brittle creep: A possible mechanism to reconcile geodetic measurements and the decay rate of aftershocks, application to the Chi-Chi earthquake, Taiwan. *Journal of Geophysical Research*, *109*, B02304. https://doi.org/10.1029/2003JB002488

Perfettini, H., Frank, W., Marsan, D., & Bouchon, M. (2018). A model of aftershock migration driven by afterslip. *Geophysical Research Letters*, *45*, 2283–2293. https://doi.org/10.1002/2017GL076287

Petersen, M. D., Moschetti, M. P., Powers, P. M., Mueller, C. S., Haller, K. M., Frankel, A. D., et al. (2014). Documentation for the 2014 update of the United States national seismic hazard maps. *U.S. Geological Survey Open-File Report 2014–1091* (243 p.). https://dx.doi.org/10.3133/ofr20141091.

Reasenberg, P. A., & Jones, L. M. (1994). Earthquake aftershocks: Update. *Science*, *265*(5176), 1251–1252. https://doi.org/10.1126/science.265.5176.1251

Ross, Z. E., Rollins, C., Cochran, E. S., Hauksson, E., Avouac, J.-P., & Ben-Zion, Y. (2017). Aftershocks driven by afterslip and fluid pressure sweeping through a fault-fracture. *Geophysical Research Letters*, *44*, 8260–8267. https://doi.org/10.1002/2017GL074634

Schmeelk, D., Bendick, R., Stickney, M., & Bomberger, C. (2017). Kinematic evidence for the effect of changing plate boundary conditions on the tectonics of the northern U.S. Rockies. *Tectonics*, *36*, 1090–1102. https://doi.org/10.1002/2016TC004427

Shapiro, S. A., Huenges, E., & Borm, G. (1997). Estimating the crust permeability from fluid-injection-induced seismic emission at the KTB site. *Geophysical Journal International*, *131*(2), F15–F18. https://doi.org/10.1111/j.1365-246X.1997.tb01215.x

Shelly, D. R., Hill, D. P., Massin, F., Farrell, J., Smith, R. B., & Taira, T. (2013). A fluid-driven earthquake swarm on the margin of the Yellowstone caldera. *Journal of Geophysical Research: Solid Earth*, *118*, 1–15. https://doi.org/10.1002/jgrb.50362

Smith, R. B., & Arabasz, W. J. (1991). Seismicity of the Intermountain Seismic Belt. In D. B. Slemmons, et al. (Eds.), *Neotectonics of North America: Geological Society of America, decade map* (Vol. 1, pp. 185–228). Boulder, CO: Geological Society of America.

Smith, R. B., Arabasz, W. J., Pechmann, J. C., & Richins, W. D. (1983). Earthquake hazards and prediction research in the Wasatch Front/Southern Intermountain Seismic Belt, final technical report, United States Geological Survey Contract No. 14–08–0001-21184, 21 p.

Tajima, F., & Kanamori, H. (1985). Global survey of aftershock area expansion patterns. *Physics of the Earth and Planetary Interiors*, *40*(2), 77–134. https://doi.org/10.1016/0031-9201(85)90066-4

Talley, J. H., & Cloud, W. K. (1962). *United States earthquakes 1960*. Washington, DC: U.S. Coast and Geodetic Survey.

Trugman, D. T., & Shearer, P. M. (2017). GrowClust: A hierarchical clustering algorithm for relative earthquake relocation, with application to the Spanish Springs and Sheldon, Nevada, earthquake sequences. *Seismological Research Letters*, *88*(2A), 379–391. https://doi.org/10.1785/0220160188

U.S. Geological Survey (2017). Summary of M5.3 Soda Springs, Idaho, earthquake, https://earthquake.usgs.gov/earthquakes/eventpage/us2000aekg#executive, last accessed March 23, 2018.

Waldhauser, F. (2000). A double-difference earthquake location algorithm: Method and application to the northern Hayward fault, California. *Bulletin of the Seismological Society of America*, *90*(6), 1353–1368. https://doi.org/10.1785/0120000006

Wiens, D., & McGuire, J. J. (2000). Aftershocks of the March 9, 1994, Tonga earthquake: The strongest known deep aftershock sequence. *Journal of Geophysical Research*, *105*, 19,067–19,083.

Wong, I., Lund, W., DuRoss, C., Thomas, P., Arabasz, W., Crone, A., et al. (2016). Earthquake probabilities for the Wasatch Front the region in Utah, Idaho, and Wyoming, Utah Geological Survey, Misc. Publ. 16–3, 164 pp. (excluding appendices).